

Revealing the Electronic Structure of Silicon Intercalated Armchair Graphene Nanoribbons by Scanning Tunneling Spectroscopy

Okan Deniz,[†] Carlos Sánchez-Sánchez,[†] Tim Dumlaff,[‡] Xinliang Feng,[§] Akimitsu Narita,[‡] Klaus Müllen,[‡] Neerav Kharche,^{||} Vincent Meunier,^{||} Roman Fasel,^{†,⊥} and Pascal Ruffieux^{*,†}

[†]Empa, Swiss Federal Laboratories for Materials Science and Technology, Überlandstrasse 129, CH-8600 Dübendorf, Switzerland

[‡]Max Planck Institute for Polymer Research, Ackermannweg 10, D-55128 Mainz, Germany

[§]Chair of Molecular Functional Materials, Department of Chemistry and Food Chemistry, Technische Universität Dresden, Mommsenstrasse 4, D-01062 Dresden, Germany

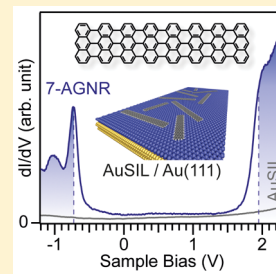
^{||}Department of Physics, Applied Physics, and Astronomy, Rensselaer Polytechnic Institute, Troy, New York 12180, United States

[⊥]Department of Chemistry and Biochemistry, University of Bern, Freiestrasse 3, CH-3012 Bern, Switzerland

Supporting Information

ABSTRACT: The electronic properties of graphene nanoribbons grown on metal substrates are significantly masked by the ones of the supporting metal surface. Here, we introduce a novel approach to access the frontier states of armchair graphene nanoribbons (AGNRs). The in situ intercalation of Si at the AGNR/Au(111) interface through surface alloying suppresses the strong contribution of the Au(111) surface state and allows for an unambiguous determination of the frontier electronic states of both wide and narrow band gap AGNRs. First-principles calculations provide insight into substrate induced screening effects, which result in a width-dependent band gap reduction for substrate-supported AGNRs. The strategy reported here provides a unique opportunity to elucidate the electronic properties of various kinds of graphene nanomaterials supported on metal substrates.

KEYWORDS: Graphene nanoribbon, intercalation, surface alloying, scanning tunneling spectroscopy, density functional theory, screening



The absence of a band gap in graphene entails severe limitations for its use in electronic switching devices where a high on/off ratio is required.¹ Since the discovery of graphene, many efforts have thus been devoted to overcome this limitation by either directly inducing a band gap in graphene^{2,3} or by creating sophisticated heterostructures allowing one to increase the on/off ratio in related switching devices.^{4,5} Among the proposed strategies, the use of quasi-one-dimensional (1D) graphene nanoribbons (GNRs) has attracted substantial attention as GNRs exhibit a width-dependent band gap due to quantum confinement.⁶ Several schemes, based on top-down^{7,8} and bottom-up⁹ approaches, have been proposed regarding GNR fabrication. However, atomic precision in ribbon width and edge structure, and thus a well-defined specific band gap, has only been achieved by the bottom-up approach that is based on the surface-assisted polymerization and subsequent cyclodehydrogenation of specifically designed molecular precursors, as first reported for the synthesis of armchair GNRs of width $N = 7$ (7 carbon atoms across the ribbon, 7-AGNRs).⁹ Recently, this approach has proven successful for the fabrication of AGNRs of different width (3-AGNR,^{10,11} 5-AGNR,^{12,13} 9-AGNR,¹⁴ 13-AGNR,¹⁵ 14-AGNR,¹⁶ 21-AGNR¹⁶) and related heterostructures^{17,18} as well as GNRs with other edge topologies.^{19–21}

While the bottom-up approach yields GNRs with the atomic precision needed for the deterministic definition of their

electronic properties, an important limitation arises from the presence of the metallic growth substrate used for their synthesis. Metal substrates are needed as template and catalyst for the surface-assisted synthesis steps, but they also have the adverse effect to prevent direct exploitation of the semi-conducting electronic properties of the GNRs. In addition, a detailed determination of the electronic structure of the as-grown GNRs is made difficult due to screening effects and the overlap of the GNR states with surface states of the (111) surfaces of Au, Ag, and Cu, which are typically used as growth substrates. This limitation becomes particularly severe for narrower band gap GNRs in which the determination of the frontier states by scanning tunneling spectroscopy (STS) has proven ambiguous.^{12–15,22,23}

One approach to circumvent the limitations imposed by the presence of the metal substrate is the ex situ transfer of the GNRs onto an insulator,^{17,24} a venture that involves the use of harsh chemicals and ambient conditions which can potentially modify and contaminate the GNRs. Alternatively, the in situ introduction of an ultrathin layer of an insulator or semiconductor material at the GNR/metal interface (Figure 1) by intercalation would allow to modify the supporting substrate in

Received: November 11, 2016

Revised: March 10, 2017

Published: March 16, 2017

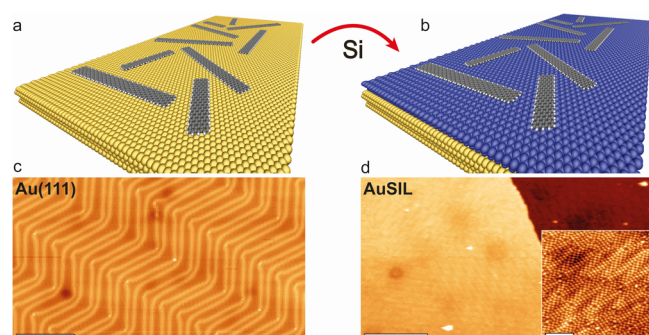


Figure 1. In situ Si intercalation approach for graphene nanoribbons synthesized on metal substrates. (a) The 7-AGNRs on Au(111) and (b) 7-AGNRs on AuSIL formed via Si intercalation. (c) STM images of clean Au(111) surface ($U = -1.5$ V $I = 80$ pA), and (d) AuSIL ($U = 1$ V $I = 70$ pA). The inset of (d) shows the STM image of AuSIL at atomic resolution ($U = 1$ V $I = 70$ pA). Scale bars of the STM images and the inset are 20 and 5 nm, respectively.

a controlled way and might eventually open routes for the efficient electronic decoupling of the GNRs. Here, we demonstrate that silicon intercalation at the GNR/Au(111) interface can lead to the controlled creation of a gold silicide (AuSIL) buffer between Au and the AGNRs, which remain structurally intact. Most importantly, this allows for an unambiguous determination of the frontier states and thus of the electronic band gaps of atomically precise AGNRs by means of STS. The measured band gaps of the substrate-

supported AGNRs are significantly smaller than the calculated quasiparticle values of isolated AGNR, thereby revealing a width-dependent band gap reduction. This substrate screening effect is elucidated by first-principles calculations and a recently presented screening model that takes GNR's width and polarizability into account.²⁵

The strategy used for the intercalation process is illustrated in Figure 1. In a first step, we synthesize AGNRs on a Au(111) substrate (Figure 1a) under ultrahigh vacuum conditions, following the on-surface polymerization and cyclodehydrogenation procedure reported earlier.⁹ After GNR growth, Si is intercalated at the AGNR/Au interface through Si deposition onto the substrate (Figure 1b) aiming for controlled modification of the underlying surface.

In order to examine the morphology of Si-covered Au, we focus on Si deposition on a bare Au(111) substrate prior to the AGNR intercalation experiments. Upon Si deposition on Au(111) held at 475 K, a Au–Si alloy^{26,27} (Figure 1d) is formed at the surface as expected from the Au–Si phase diagram.²⁸ However, a clear-cut determination of the total amount of deposited Si is nontrivial due to significant Si diffusion into the Au(111) subsurface region, which results in intermixed gold silicide layers that extend into bulk Au.²⁷ Therefore, we refer 1 monolayer (ML) AuSIL coverage to the amount of deposited Si needed to entirely saturate the gold silicide reported in Supporting Figure S1. The corresponding surface structure, shown in the inset of Figure 1d, appears to be similar to the earlier reported Au_{2.43}Si structure,²⁷ because it

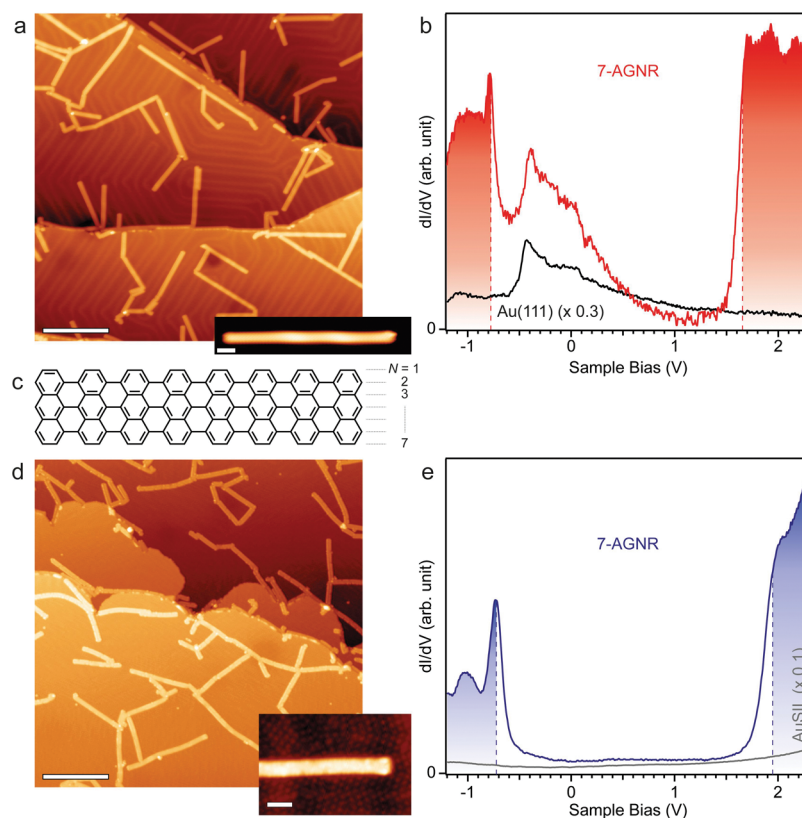


Figure 2. The 7-AGNRs before and after Si intercalation. (a) STM image ($U = -1.1$ V $I = 50$ pA) and (b) dI/dV spectra of 7-AGNR on Au(111). The GNR spectrum is dominated by the Au(111) surface state. A structural model of the 7-AGNR is shown in (c). (d,e) The 7-AGNRs on 1 ML AuSIL after Si intercalation at the AGNR/Au interface. (d) STM image ($U = -1.5$ V $I = 50$ pA). The inset of (d) shows that 7-AGNRs are found intact after Si intercalation. (e) dI/dV spectra of a 7-AGNR and the AuSIL surface. Scale bars of the STM images and the insets are 20 and 2 nm, respectively.

exhibits the same low energy electron diffraction patterns (not shown). The as-grown AuSIL forms extended flat terraces, as seen in Figure 1d. We also observe that the AuSIL is remarkably free of Si clusters, which indicates efficient alloying at this ultralow thickness regime. Most importantly in the present context, the resulting AuSIL alloy does not feature any low-energy surface state in STS and thus it is a promising candidate to substitute Au(111) as supporting substrate for GNRs.

The 7-AGNR on Au(111) has been selected as a model system for the Si intercalation studies discussed here because its electronic properties have been extensively investigated and are now well understood.^{29,30} The 7-AGNRs on the clean Au(111) are shown in Figure 2a. It is clearly seen that differential conductance dI/dV spectra recorded on 7-AGNRs reveal significant substrate contributions, as reported in literature.²⁹ The most prominent contribution stems from the Au(111) surface state with an onset at around -0.4 V, as shown in Figure 2b. GNRs on (111) metal surfaces are significantly dominated by the metal's surface state which decays relatively slowly into the vacuum in comparison to some GNR states that are found only in the vicinity of the ribbon.¹⁶ As a result, these rapidly decaying GNR states might be completely obscured by substrate contribution in an STS measurement.³⁰ An unambiguous assignment of the GNR-related electronic states requires spatially resolved dI/dV spectra²⁹ as well as a detailed understanding of the out-of-plane extension of the GNR-related electronic features.³⁰ On the basis of such an analysis, we find the valence band maximum (VBM) at -0.8 eV and the conduction band minimum (CBM) at 1.6 eV for the 7-AGNR (Figure 2c) on Au(111), resulting in a band gap of 2.4 eV. This band gap is significantly smaller than the predicted quasiparticle band gap of 3.8 eV for free-standing 7-AGNRs.³¹ The reduction in band gap has been attributed to the aforementioned substrate screening effect²⁹ and indeed the experimentally observed band gap is in good agreement with theoretical calculations that include screening by the substrate.²⁵

As mentioned above, the proposed strategy for the controlled modification of the surface layers of the growth substrate is the formation of a thin gold silicide via Si intercalation at the 7-AGNR/Au(111) interface. Figure 2d shows an STM image after intercalation of 1 ML of AuSIL by Si deposition on the substrate held at 475 K. We observe a strong modification of the surface in STM images, notably with the disappearance of the Au(111) herringbone reconstruction and the presence of a uniform AuSIL layer all over the surface, including the area below the GNRs (Figure 2d). Most importantly, the quality of the GNRs as well as their length distribution is preserved upon Si intercalation. Owing to the comparatively high corrugation and large periodicity of the underlying AuSIL surface, the apparent shape of the 7-AGNRs is significantly modulated so that the underlying atomic structure of the AuSIL is partially visible through the ribbons (see the Supporting Figure S2) and GNR edges appear to be less smooth. Beside this apparent change of the edge structure we observe minor decoration of the edges with Si adatoms as it is indicated in Supporting Figure S2. The intercalation process here can be rationalized in a manner similar to the one governing Si intercalation under graphene^{32–36} in which the consensus is that Si intercalates through defects of graphene. In the case of GNRs, the substrate is covered by narrow graphene stripes, which opens a substantial area for incoming Si atoms. Intercalation of Si under GNRs is thus much more efficient than under graphene.

In addition to the modified surface morphology of the AuSIL, dI/dV spectra recorded on the AuSIL (Figure 2e) reveal a complete quenching of the Au surface state and an overall featureless density of states (DOS) in the energy range of interest, that is, the 7-AGNR frontier states. This is most clearly evidenced by the direct comparison of dI/dV spectra recorded on a mixed sample where sub-ML Si intercalation allows to investigate both 7-AGNRs/Au(111) and 7-AGNRs/AuSIL within a few nanometers distance (Supporting Figure S3). While the dI/dV spectrum recorded on the Au(111)-adsorbed 7-AGNR reveals contributions from ribbon and substrate's surface state, the corresponding spectrum on the AuSIL-supported 7-AGNR reveals a featureless band gap region with well-defined contributions of the frontier GNR states.

Because of the suppression of the Au(111) surface state through AuSIL formation, dI/dV spectra of 7-AGNRs on AuSIL exhibit well-defined features at -0.7 and 2.0 eV, which can be directly assigned to VBM and CBM, respectively (Figure 2e). Similar as for Au(111) supported 7-AGNR, the intercalated 7-AGNR shows consistent VBM and CBM positions, which is evidenced by a series of dI/dV spectra recorded along the GNR edge (see Supporting Figure S4). Even for the case of Si edge adsorption, VBM and CBM positions remain constant and only their intensity is modulated owing to the modified apparent shape and related variation of the relative tip height at the Si adsorption site. The corresponding band gap of 2.7 eV is closer to the theoretically predicted band gap of the free-standing 7-AGNR (Table 1),

Table 1. Comparison of Experimental and Theoretical Band Gap Values (in eV) of Free-Standing and Substrate-Supported N-AGNRs

	experiment	theory	
	substrate-supported	free-standing ^a	substrate-supported
7-AGNR	2.7	3.79	2.60
9-AGNR	1.5	2.29	1.40
14-AGNR	0.2	0.71	0.23
18-AGNR	0.9	1.43	0.82
21-AGNR	0.7	1.27	0.73

^aReference 44.

indicating a significantly lower screening by the silicide surface. Most importantly, the low and featureless AuSIL contribution to the dI/dV spectra allows for an unambiguous assignment of the GNR-related low energy states that holds particular importance for the characterization of GNRs with narrow band gaps.

Following the successful Si intercalation for 7-AGNRs, we expand our study to a number of additional AGNRs of different widths (and hence different magnitudes of the band gap). AGNRs are classified into three different families depending on the number of C atoms (N) across the ribbon, namely $N = 3p$, $3p + 1$ and $3p + 2$, where p is an integer.³¹ While the band gap magnitude of the three families differs significantly, their width-dependence is similar that the band gap decays with $1/(N + N_0)$, N_0 being a small constant.³¹ Regarding the wider AGNRs with narrower band gaps, the presence of the (111) metal surface imposes a particular restriction for accessing the GNR-related low energy states since these may overlap energetically with the surface state. This limitation makes Si intercalation an ideal approach to probe the frontier states of the narrow band gap AGNRs.

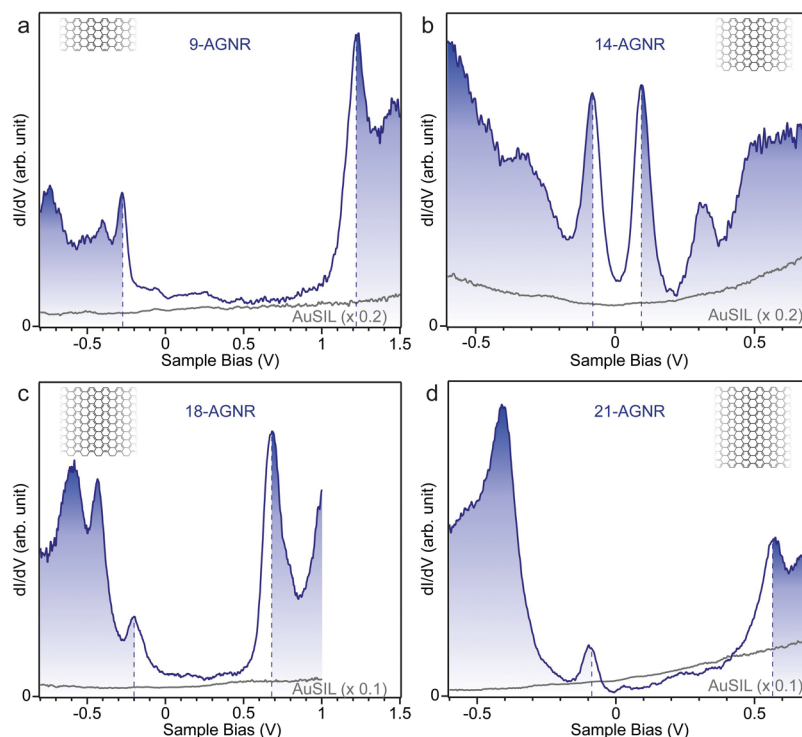


Figure 3. Differential conductance dI/dV spectra for different N -AGNRs on the Si intercalated Au(111) substrate. (a) 9-AGNR, (b) 14-AGNR, (c) 18-AGNR, and (d) 21-AGNR on AuSIL/Au(111). The insets give the structural model of the corresponding AGNR.

A significantly narrower band gap is expected for the 9-AGNR ($3p$) compared to the 7-AGNR ($3p + 1$).³¹ The growth procedure as well as morphological and electronic properties of the 9-AGNR on Au(111) have been studied in detail and reported elsewhere.¹⁴ For the as-grown 9-AGNRs on Au(111) we find a band gap of 1.4 eV by STS.¹⁴ In contrast to the nontrivial determination of the 9-AGNR band gap on Au(111), we clearly resolve the VBM and CBM at -0.3 and 1.2 eV, respectively (shown in Figure 3a and Supporting Figure S5) as soon as Si is intercalated between the 9-AGNRs and the Au(111) growth substrate. The resulting band gap of 1.5 eV for 9-AGNRs on AuSIL is slightly wider than the one observed on Au(111). The increase in band gap upon Si intercalation observed for both the 7- and 9-AGNR demonstrates clearly that AuSIL formation modifies the screening properties of the substrate.

Further examples of AGNRs with increased width have been achieved via cross-dehydrogenative coupling (lateral fusion) of 7- and 9-AGNRs, which results in AGNRs of multiple width with respect to the original AGNRs.¹⁶ Si intercalation for these multiple AGNRs is found to be equally efficient as for 7- and 9-AGNRs (Supporting Figure S6). Figure 3b–d shows dI/dV spectra recorded on 14-AGNRs (two fused 7-AGNRs), 18-AGNRs (two fused 9-AGNRs), and 21-AGNRs (three fused 7-AGNRs), respectively, and reveals clearly resolved GNR-related spectral features that can be assigned to the VBM and CBM of the ribbons. As expected, the corresponding band gaps vary significantly as a function of the GNR width and to which band gap family they belong. We find band gap values of 0.2 eV (14-AGNR, $3p + 2$ family), 0.9 eV (18-AGNR, $3p$ family) and 0.7 eV (21-AGNR, $3p$ family), which qualitatively confirm the theoretical predictions for the family- and width-dependent band gap magnitude.³¹

The experimentally determined band gaps of AGNRs supported on the AuSIL substrate are compared with the quasiparticle band gaps of free-standing AGNRs calculated using the GW approximation in Table 1. It is now well established that the presence of a substrate has a marked effect on the reduction of the band gap of low-dimensional nanostructures such as GNRs.³⁷ This reduction is caused by the substrate-induced weakening of the effective electrostatic potential due to screening effects, which in turn lead to a narrowing of the band gap. This effect is a nonlocal phenomenon that cannot be captured within DFT using standard exchange correlation functionals. However, by correcting the behavior of the long-range potential from an exponential decay (i.e., shortcoming of DFT) to the appropriate $-1/z$ decay, the so-called image-charge model is able to account for this effect, albeit in a semiquantitative manner. The image-charge model also accounts for the dielectric properties of the substrate and correctly predicts that band gap reduction is significantly more pronounced for metals compared to semiconducting substrates. However, the classical image-charge model^{29,38} does not account for the properties (structural and electronic) of the adsorbates and therefore predicts same band gap reduction regardless of the type and size of the supported GNR. This contradicts with the experimental data reported in Table 1, which clearly shows that the substrate-supported AGNRs exhibit a width-dependent band gap reduction. This is not surprising, because the polarizability of strongly confined nanostructures is very sensitive to the details of their structure. It follows that the reduction of the band gap due to the presence of the substrate should be understood in terms of the effective image potential at the location of the GNR, taking into account not only the properties of the substrate and the position of the GNR relative to the substrate but also the properties of the GNR itself. This

effect has been recently formalized theoretically by Kharche and Meunier, who also provided a computational framework to evaluate this effect.²⁵ In the following, we refer to this new procedure as the advanced image-charge model.

In practice, we adopt a two-step computational approach.^{25,37} It should be emphasized that the image-charge model only includes effects related to the substrate-induced gap reduction. Indeed, the renormalization of the band gap of an isolated material is due to the known propensity of DFT (in its local and semilocal descriptions) to strongly underestimate band gaps, especially in reduced dimensions. Thus, the first step is to correct this effect, before considering any effect of the presence of a substrate. This can be done by first calculating the quasiparticle energy levels of the GNR in the isolated configuration within the GW approach. The second step is to correct the quasiparticle energy levels due to substrate screening within the advanced image-charge model.²⁵ In principle, this approach provides a fully first-principles framework for predicting the quasiparticle electronic structure of substrate-supported GNRs in weak interaction with the substrate. However, in the case of Si incorporated Au(111) the accurate determination of the image-plane position of the substrate and the distance between the substrate and the AGNRs is made difficult by the fact that the precise atomic structure of the Si incorporated Au(111) (the AuSIL) is unknown. To circumvent this limitation, we use the distance between the AGNRs and the image-plane position (h) as a fitting parameter. A good agreement with the experimental results is obtained for $h = 2.5$ Å. The fact that a single value of h is able to reproduce results for different AGNRs shows that it is indeed a property of the image plane, independent of the supported GNR, as expected. Further details of the computational methods are provided in the [Methods](#) section.

Figure 4 presents the calculated as well as the experimentally determined band gaps of AGNRs supported on the Si incorporated Au(111) substrate as a function of nanoribbon width, where a good agreement is seen for all three families of AGNRs. The band gap reduction relative to the free-standing

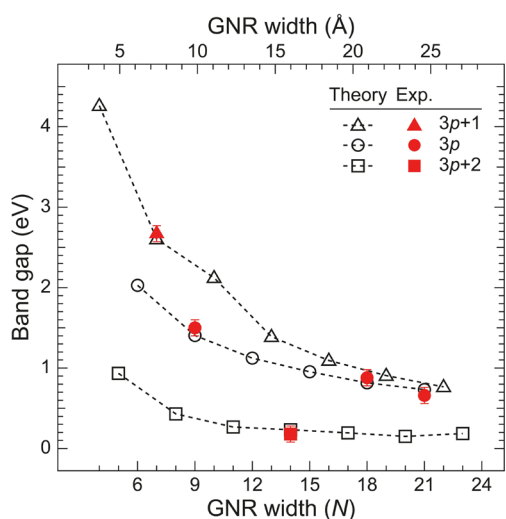


Figure 4. Comparison of experimentally determined band gaps of AGNRs on 1 ML AuSIL/Au(111) obtained by Si intercalation (red) and the calculated band gaps of the AGNRs supported on a model Au₃Si substrate (black). Details of the theoretical calculation are given in the [Computational Methods](#) section.

AGNRs is shown separately in Figure S7 in the [Supporting Information](#). The clear width-dependence of the band gap reduction seen in [Supporting Figure S7](#) is attributed to the larger polarizability of wider AGNRs as illustrated in [Supporting Figure S8](#) in the [Supporting Information](#). This can be understood by the fact that wider nanoribbons make it easier for charge to redistribute and respond to the presence of an external field (in this case, the image-charge potential). This argument also explains why the intrinsic band gap of wider GNRs in a given family is less affected by the presence of the substrate. In addition, because the electronic properties of GNRs vary between GNR families we also expect the band gap reduction to be family dependent (i.e., narrow gap GNRs should be less affected than wider gap GNRs, regardless of family, for similar width). Within each of the three families ($3p$, $3p + 1$, and $3p + 2$) of AGNRs, polarizability scales linearly as a function of $1/E_g^2$, where E_g is the DFT band gap. As expected, our model determines that the polarizability of each of the three families of AGNRs shows a different scaling behavior with respect to the band gap ([Supporting Figure S8](#)), broadly in the order $3p + 2 > 3p > 3p + 1$. Within each of the three families, wider AGNRs, owing to their larger polarizabilities, exhibit stronger internal screening. Hence, the external screening by the substrate has a weaker effect, leading to smaller substrate-induced band gap reduction. When comparing across the families, the magnitude of the band gap reduction due to the substrate screening broadly follows the order $3p + 1 > 3p > 3p + 2$ ([Supporting Figure S7](#)), which is in reverse order from polarizability strength.

In conclusion, we have reported an ultraclean in situ intercalation approach for probing the electronic states of atomically precise AGNRs. We have demonstrated that Si intercalation can be successfully applied to various AGNRs on Au(111) and allows for an unambiguous determination of the frontier states and hence of the AGNR band gap. In comparison to the case of metal-supported AGNRs, we find an increase of the band gap for AGNRs on the AuSIL. On the basis of first-principles calculations, we have discussed the impact of screening by the substrate on the AGNR band gap and how it depends on the width of the AGNR. Narrower AGNRs experience larger band gap reduction due to substrate screening as a result of their weaker internal screening response. Consequently, one can extrapolate the behavior of the present examples toward the GNRs with different widths and other edge topology such as zigzag edges or chiral GNR morphologies. Most importantly, these findings open an avenue to controllably alter properties of the substrate, which is expected to be a key step in the development of in situ processes for the electronic decoupling of GNRs. Such decoupling would be a prerequisite for accessing the intrinsic semiconducting properties of GNRs and allowing the realization of GNR-based electronic devices.

Methods. Experimental Methods. All experiments were performed in an ultrahigh vacuum low-temperature STM system (ScientaOmicron) with a base pressure below 2×10^{-10} mbar. The Au(111) crystal (MaTeck GmbH) was cleaned by repetitive Ar⁺ sputtering (1 keV) and annealing (725 K) cycles. Sputtering at elevated temperature (about 675 K) was performed as the last step in order to prevent any segregation of Si from the Au bulk. On-surface synthesis of 7-AGNR and 9-AGNR are explained elsewhere.^{9,14} Wider derivatives (14-AGNR, 18-AGNR, and 21-AGNR) of 7-AGNR and 9-AGNR were prepared by rising up the sample temperature beyond the

needed cyclodehydrogenation temperature (e.g. to 720 K), which allows for the formation of higher order AGNRs by cross-dehydrogenative coupling of the originally formed ribbons.¹⁶ Following GNR fabrication, Si was thermally evaporated from a Si wafer (n-type, 1–8 ohm.cm) stripe ($20 \times 2 \times 0.5$ mm) by a homemade direct current evaporator on Au(111) held at 475 K, measured by an infrared pyrometer (Optris GmbH – Model CT-laser) with emissivity of 0.1. Heating of the substrate was immediately stopped after the deposition was completed. The AuSIL coverage was controlled by STM, performed at 77 or 5 K. An etched tungsten tip was used for STM and STS measurements. The scanning tunneling dI/dV spectra were recorded at 5 K, using the lock-in technique ($U_{rms} = 20$ mV) at constant tip height. Prior to the acquisition of dI/dV spectra, the combination of controlled tip indentation in AuSIL and voltage pulses (up to 10 V) was applied until a consistent spectrum was recorded on GNRs. The parameters of the STS spectra of intercalated GNRs were -1.2 V, 500 pA for 7-AGNR, -0.8 V, 700 pA for 9-AGNR, -0.6 V, 400 pA for 14-AGNR, -0.8 V, 400 pA for 18-AGNR, and -0.6 V, 400 pA for 21-AGNR. VBM and CBM of GNRs were determined as follows: if the state appeared as a well-defined peak, we have taken the peak position as the energy of that state and if the state appeared as a steplike contribution in dI/dV , VBM and CBM were determined according to the procedure described in ref 30.

Computational Methods. DFT calculations were performed with the Vienna Ab initio simulation package (VASP)^{39,40} using the projector augmented wave (PAW) method⁴¹ and the PBE exchange-correlation functional.⁴² The longitudinal dielectric constant (ϵ) of AGNRs is calculated using density functional perturbation theory (DFPT).⁴³ We use a supercell size such that the closest distance between adjacent GNRs is at least 15 Å. We use a plane-wave cutoff of 400 eV, and a $1 \times 1 \times n_{kz}$ k -point grid with $n_{kz} = 24$. Polarizability (α) of AGNRs is calculated using the 1D Clausius–Mossotti expression $\alpha = (A/4\pi)(\epsilon - 1)$, where A is the cross-sectional area of the supercell. The distance between the AGNRs and the image-plane position of the substrate (h) is taken to be $h = 2.5$ Å. Using these values of α and h , we calculate the band gap reduction ($\Delta E_{g,model}^{QP}$) due to the substrate screening using the advanced image-charge model presented in ref 25. Finally, we calculate the quasiparticle band gaps of the substrate-supported AGNRs using $E_{g,ads}^{QP} = E_{g,iso}^{GW} - QP + \Delta E_{g,model}^{QP}$, where $E_{g,ads}^{QP}$ is the quasiparticle band gap of the substrate-supported AGNRs and $E_{g,iso}^{GW} - QP$ is the GW quasiparticle band gap of free-standing AGNRs, which is taken from ref 44.

■ ASSOCIATED CONTENT

■ Supporting Information

The Supporting Information is available free of charge on the ACS Publications website at DOI: 10.1021/acs.nanolett.6b04727.

STM images show the thickness calibration of AuSIL, the appearance of AuSIL under 21-AGNR, and the corresponding positions of the spectra in Figures 2e and 3a–d. Moreover, STS spectra of partially Si intercalated 7-AGNR, series of spectra on a line along the Si intercalated 7-AGNR and the dI/dV maps of Si intercalated 9-AGNR are exhibited. Calculated quasiparticle band gaps of AGNRs as a function of ribbon width together with the GW quasiparticle band gaps of isolated

AGNRs are given. Additionally, the polarizability values of 3p, 3p+1 and 3p+2 family AGNRs with respect to $1/E_g^2$ are reported(PDF)

■ AUTHOR INFORMATION

Corresponding Author

*E-mail: pascal.ruffieux@empa.ch.

ORCID

Okan Deniz: 0000-0001-8634-8849

Carlos Sánchez-Sánchez: 0000-0001-8644-3766

Akimitsu Narita: 0000-0002-3625-522X

Klaus Müllen: 0000-0001-6630-8786

Pascal Ruffieux: 0000-0001-5729-5354

Present Address

(C.S.S.) Instituto de Ciencia de Materiales de Madrid (ICMM-CSIC), Sor Juana Inés de la Cruz 3, 28049 Madrid, Spain.

Author Contributions

All authors have given approval to the final version of the manuscript. O.D. performed the experiments. T.D. prepared precursor molecules under the supervision by X.F., A.N., and K.M. N.K. and V.M. calculated the band gaps of AGNRs. O.D., C.S.S., R.F., and P.R. conducted the research, analyzed the data, and cowrote the manuscript.

Notes

The authors declare no competing financial interest.

■ ACKNOWLEDGMENTS

This work has been supported by the Swiss National Science Foundation, the Office of Naval Research BRC program, and the European Commission Graphene Flagship (No. CNECT-ICT-604391). C.S.S. is grateful to Ministerio de Economía y Competitividad for financial support via the Juan de la Cierva Incorporación Grant (IJCI-2014-19291, cofunded by the European Investment Bank).

■ REFERENCES

- (1) Novoselov, K. S. *Science* **2004**, 306 (5696), 666–669.
- (2) Castro, E. V.; Novoselov, K. S.; Morozov, S. V.; Peres, N. M. R.; dos Santos, J. M. B. L.; Nilsson, J.; Guinea, F.; Geim, A. K.; Neto, A. H. C. *Phys. Rev. Lett.* **2007**, 99 (21), 216802.
- (3) Oostinga, J. B.; Heersche, H. B.; Liu, X.; Morpurgo, A. F.; Vandersypen, L. M. K. *Nat. Mater.* **2008**, 7 (2), 151–157.
- (4) Britnell, L.; Gorbachev, R. V.; Jalil, R.; Belle, B. D.; Schedin, F.; Mishchenko, A.; Georgiou, T.; Katsnelson, M. I.; Eaves, L.; Morozov, S. V.; Peres, N. M. R.; Leist, J.; Geim, A. K.; Novoselov, K. S.; Ponomarenko, L. A. *Science* **2012**, 335 (6071), 947–950.
- (5) Yang, H.; Heo, J.; Park, S.; Song, H. J.; Seo, D. H.; Byun, K.-E.; Kim, P.; Yoo, I.; Chung, H.-J.; Kim, K. *Science* **2012**, 336 (6085), 1140–1143.
- (6) Barone, V.; Hod, O.; Scuseria, G. E. *Nano Lett.* **2006**, 6 (12), 2748–2754.
- (7) Bai, J.; Duan, X.; Huang, Y. *Nano Lett.* **2009**, 9 (5), 2083–2087.
- (8) Jiao, L.; Xie, L.; Dai, H. *Nano Res.* **2012**, 5 (4), 292–296.
- (9) Cai, J.; Ruffieux, P.; Jaafar, R.; Bieri, M.; Braun, T.; Blankenburg, S.; Muoth, M.; Seitsonen, A. P.; Saleh, M.; Feng, X.; Muellen, K.; Fasel, R. *Nature* **2010**, 466 (7305), 470–473.
- (10) Vasseur, G.; Fagot-Revurat, Y.; Sicot, M.; Kierren, B.; Moreau, L.; Malterre, D.; Cardenas, L.; Galeotti, G.; Lipton-Duffin, J.; Rosei, F.; Di Giovannantonio, M.; Contini, G.; Le Fèvre, P.; Bertran, F.; Liang, L.; Meunier, V.; Perepichka, D. F. *Nat. Commun.* **2016**, 7, 10235.
- (11) Vasseur, G.; Abadia, M.; Miccio, L. A.; Brede, J.; Garcia-Lekue, A.; de Oteyza, D. G.; Rogero, C.; Lobo-Checa, J.; Ortega, J. E. *J. Am. Chem. Soc.* **2016**, 138 (17), 5685–5692.

- (12) Kimouche, A.; Ervasti, M. M.; Drost, R.; Halonen, S.; Harju, A.; Joensuu, P. M.; Sainio, J.; Liljeroth, P. *Nat. Commun.* **2015**, *6*, 10177.
- (13) Zhang, H.; Lin, H.; Sun, K.; Chen, L.; Zaganyarski, Y.; Aghdassi, N.; Duhm, S.; Li, Q.; Zhong, D.; Li, Y.; Müllen, K.; Fuchs, H.; Chi, L. *J. Am. Chem. Soc.* **2015**, *137* (12), 4022–4025.
- (14) Talirz, L.; Söde, H.; Dumschlaff, T.; Wang, S.; Sanchez-Valencia, J. R.; Liu, J.; Shinde, P.; Pignedoli, C. A.; Liang, L.; Meunier, V.; Plumb, N. C.; Shi, M.; Feng, X.; Narita, A.; Müllen, K.; Fasel, R.; Ruffieux, P. *ACS Nano* **2017**, *11*, 1380.
- (15) Chen, Y.-C.; de Oteyza, D. G.; Pedramrazi, Z.; Chen, C.; Fischer, F. R.; Crommie, M. F. *ACS Nano* **2013**, *7* (7), 6123–6128.
- (16) Huang, H.; Wei, D.; Sun, J.; Wong, S. L.; Feng, Y. P.; Neto, A. H. C.; Wee, A. T. S. *Sci. Rep.* **2012**, *2*, 983.
- (17) Cai, J.; Pignedoli, C. A.; Talirz, L.; Ruffieux, P.; Söde, H.; Liang, L.; Meunier, V.; Berger, R.; Li, R.; Feng, X.; Müllen, K.; Fasel, R. *Nat. Nanotechnol.* **2014**, *9* (11), 896–900.
- (18) Chen, Y.-C.; Cao, T.; Chen, C.; Pedramrazi, Z.; Haberer, D.; de Oteyza, D. G.; Fischer, F. R.; Louie, S. G.; Crommie, M. F. *Nat. Nanotechnol.* **2015**, *10* (2), 156–160.
- (19) Liu, J.; Li, B.-W.; Tan, Y.-Z.; Giannakopoulos, A.; Sanchez-Sanchez, C.; Beljonne, D.; Ruffieux, P.; Fasel, R.; Feng, X.; Müllen, K. *J. Am. Chem. Soc.* **2015**, *137* (18), 6097–6103.
- (20) Ruffieux, P.; Wang, S.; Yang, B.; Sánchez-Sánchez, C.; Liu, J.; Dienel, T.; Talirz, L.; Shinde, P.; Pignedoli, C. A.; Passerone, D.; Dumschlaff, T.; Feng, X.; Müllen, K.; Fasel, R. *Nature* **2016**, *531* (7595), 489–492.
- (21) de Oteyza, D. G.; García-Lekue, A.; Vilas-Varela, M.; Merino-Díez, N.; Carbonell-Sanromà, E.; Corso, M.; Vasseur, G.; Rogero, C.; Guitián, E.; Pascual, J. I.; Ortega, J. E.; Wakayama, Y.; Peña, D. *ACS Nano* **2016**, *10* (9), 9000–9008.
- (22) Vo, T. H.; Perera, U. G. E.; Shekhirev, M.; Mehdi Pour, M.; Kunkel, D. A.; Lu, H.; Gruverman, A.; Sutter, E.; Cotlet, M.; Nykypanchuk, D.; Zahl, P.; Enders, A.; Sinitskii, A.; Sutter, P. *Nano Lett.* **2015**, *15* (9), 5770–5777.
- (23) Cloke, R. R.; Marangoni, T.; Nguyen, G. D.; Joshi, T.; Rizzo, D. J.; Bronner, C.; Cao, T.; Louie, S. G.; Crommie, M. F.; Fischer, F. R. *J. Am. Chem. Soc.* **2015**, *137* (28), 8872–8875.
- (24) Bennett, P. B.; Pedramrazi, Z.; Madani, A.; Chen, Y.-C.; de Oteyza, D. G.; Chen, C.; Fischer, F. R.; Crommie, M. F.; Bokor, J. *Appl. Phys. Lett.* **2013**, *103* (25), 253114.
- (25) Kharche, N.; Meunier, V. *J. Phys. Chem. Lett.* **2016**, *7* (8), 1526–1533.
- (26) Green, A. K.; Bauer, E. *J. Appl. Phys.* **1976**, *47* (4), 1284–1291.
- (27) Green, A. K.; Bauer, E. *J. Appl. Phys.* **1981**, *52* (8), 5098–5106.
- (28) Okamoto, H.; Massalski, T. B. *Bull. Alloy Phase Diagrams* **1983**, *4* (2), 190–198.
- (29) Ruffieux, P.; Cai, J.; Plumb, N. C.; Patthey, L.; Prezzi, D.; Ferretti, A.; Molinari, E.; Feng, X.; Müllen, K.; Pignedoli, C. A.; Fasel, R. *ACS Nano* **2012**, *6* (8), 6930–6935.
- (30) Söde, H.; Talirz, L.; Gröning, O.; Pignedoli, C. A.; Berger, R.; Feng, X.; Müllen, K.; Fasel, R.; Ruffieux, P. *Phys. Rev. B: Condens. Matter Mater. Phys.* **2015**, *91* (4), 45429.
- (31) Yang, L.; Park, C.-H.; Son, Y.-W.; Cohen, M. L.; Louie, S. G. *Phys. Rev. Lett.* **2007**, *99* (18), 186801.
- (32) Lizzit, S.; Larciprete, R.; Lacovig, P.; Dalmiglio, M.; Orlando, F.; Baraldi, A.; Gammelgaard, L.; Barreto, L.; Bianchi, M.; Perkins, E.; Hofmann, P. *Nano Lett.* **2012**, *12* (9), 4503–4507.
- (33) Mao, J.; Huang, L.; Pan, Y.; Gao, M.; He, J.; Zhou, H.; Guo, H.; Tian, Y.; Zou, Q.; Zhang, L.; Zhang, H.; Wang, Y.; Du, S.; Zhou, X.; Neto, A. H. C.; Gao, H.-J. *Appl. Phys. Lett.* **2012**, *100* (9), 93101.
- (34) Meng, L.; Wu, R.; Zhou, H.; Li, G.; Zhang, Y.; Li, L.; Wang, Y.; Gao, H.-J. *Appl. Phys. Lett.* **2012**, *100* (8), 083101.
- (35) Wang, F.; Shepperd, K.; Hicks, J.; Nevius, M. S.; Tinkey, H.; Tejeda, A.; Taleb-Ibrahimi, A.; Bertran, F.; Le Fèvre, P.; Torrance, D. B.; First, P. N.; de Heer, W. A.; Zakharov, A. A.; Conrad, E. H. *Phys. Rev. B: Condens. Matter Mater. Phys.* **2012**, *85* (16), 165449.
- (36) Xia, C.; Watcharinyanon, S.; Zakharov, A. A.; Yakimova, R.; Hultman, L.; Johansson, L. I.; Virojanadara, C. *Phys. Rev. B: Condens. Matter Mater. Phys.* **2012**, *85* (4), 045418.
- (37) Neaton, J. B.; Hybertsen, M. S.; Louie, S. G. *Phys. Rev. Lett.* **2006**, *97* (21), 216405.
- (38) Liang, L.; Meunier, V. *Phys. Rev. B: Condens. Matter Mater. Phys.* **2012**, *86* (19), 195404.
- (39) Kresse, G.; Furthmüller, J. *Phys. Rev. B: Condens. Matter Mater. Phys.* **1996**, *54* (16), 11169.
- (40) Kresse, G.; Joubert, D. *Phys. Rev. B: Condens. Matter Mater. Phys.* **1999**, *59* (3), 1758.
- (41) Blöchl, P. E. *Phys. Rev. B: Condens. Matter Mater. Phys.* **1994**, *50* (24), 17953–17979.
- (42) Perdew, J. P.; Burke, K.; Ernzerhof, M. *Phys. Rev. Lett.* **1996**, *77* (18), 3865–3868.
- (43) Gajdoš, M.; Hummer, K.; Kresse, G.; Furthmüller, J.; Bechstedt, F. *Phys. Rev. B: Condens. Matter Mater. Phys.* **2006**, *73* (4), 45112.
- (44) Zhu, X.; Su, H. *J. Phys. Chem. A* **2011**, *115* (43), 11998–12003.